Letter

Observation of self-induced spin-orbit torques in Ni-Fe layers with a vertical gradient of magnetization

Y. Hibino ,* T. Taniguchi , K. Yakushiji , H. Kubota , and S. Yuasa
Research Center for Emerging Computational Technologies (RCECT), National Institute of Advanced Industrial Science and Technology (AIST), Tsukuba, Ibaraki 305-8568, Japan

(Received 30 August 2023; accepted 23 April 2024; published 20 May 2024)

Single ferromagnetic material generates transverse spin currents via in-plane charge current application and can exert spin-orbit torques (SOTs) on its magnetization, namely, self-induced SOTs, when the inversion symmetry in the bulk and/or interface is broken. In this Letter, we experimentally demonstrate that introducing a vertical gradient of magnetization within a ferromagnet is an effective way to generate self-induced SOTs. Self-induced SOTs in Ni-Fe alloys with a magnetization gradient are studied using spin-torque ferromagnetic resonance. It is found that the gradient direction of magnetization in the Ni-Fe layer can control not only the magnitude of the SOTs but even the sign of the torques. We propose a model to analyze self-induced SOTs and reveal that the asymmetric SOT profiles within a ferromagnet due to spatial variation of the magnetic moment play a dominant role in generating efficient self-induced SOTs. Our findings provide an alternative perspective on understanding the mechanism of generating self-induced SOTs and how to enhance their torque efficiency without the use of heavy metal elements.

DOI: 10.1103/PhysRevB.109.L180409

Current-induced spin-orbit torques (SOTs) acting on ferromagnetic materials (FMs) enable ultrafast and efficient manipulation of magnetization which can be applied to the writing method of magnetoresistive random-access memory [1–4]. The driving source of the SOTs is the injection or accumulation of spin angular momentum to the FMs. The spin Hall effect in nonmagnetic materials (NMs) and the Rashba-Edelstein effect at the interfaces are typical examples of driving sources, which have been observed in the bilayer structure of FMs and NMs (NM/FM) [5,6].

Recently, it has been revealed that the charge to spin conversion phenomena, including the spin Hall effect, emerge not only in NMs but also in FMs [7–31]. The charge to spin conversion in FMs provides various unique features of SOTs. One is the emergence of unconventional SOTs which have different symmetry from SOTs induced by the spin Hall effect in NMs. This originates from the additional charge to spin conversion due to the presence of the magnetic moment [12–17]. Another unique feature is the emergence of self-induced SOTs, that is, the SOTs acting within an FM via the spin current generated within the FM itself. It has been revealed that self-induced SOTs occur in various FMs such as GaMnAs [18], Ni-Fe [19–21], Co-Pt [22–24], Fe-Pt [25–28], Fe-Mn [29], and Co-Tb [30,31]. It has also been demonstrated that self-induced SOTs can induce magnetization dynamics such as magnetization reversal [22–27,31] and oscillation [20]. These results suggest that self-induced SOTs are comparable to conventional SOTs using NM/FM bilayers, thus representing an alternative technical possibility for controlling magnetization.

Previous studies on self-induced SOTs introduced inversion asymmetry in the out of plane direction to generate finite self-induced SOTs due to the following reasons. The spin currents generated by the spin Hall effect within the FM accumulate spin angular momentum with the opposite sign at the top and bottom surfaces of the FM, resulting in self-induced SOTs with the opposite sign [Fig. 1(a)]. If the FM satisfies the inversion symmetry, the averaged spin accumulation becomes zero resulting in all the self-induced SOTs becoming zero as well. If the inversion symmetry is broken in the FM, the averaged spin accumulation remains finite resulting in finite self-induced SOTs. One of the ways to break the inversion symmetry is by introducing an asymmetric interface structure [19,22,29]. Interfacial asymmetry results in an asymmetric profile of spin accumulation, which generates finite self-induced SOTs [Fig. 1(b)]. However, because the asymmetry of spin accumulation is effective only near the interface (or surface), this method limits the efficiency of self-induced SOTs. Another way to induce structural asymmetry is to introduce a compositional gradient within the FM layer [23–31]. This method is expected to improve the efficiency of self-induced SOTs compared to the previous method. Several mechanisms of self-induced SOTs obtained via a composition gradient have been discussed so far, e.g., a spatial gradient of spin transport parameters [Fig. 1(c)], such as the spin Hall angle and resistivity, due to the disorder gradient [23–25,27], spatial gradients in the internal strain [28], and bulk-driven Rashba-Edelstein effects [26,30,31]. However, the detailed mechanisms and how to precisely control these self-induced SOTs have remained elusive.

In this Letter, we propose an alternative mechanism for the self-induced SOTs driven by a composition gradient: the presence of a vertical gradient of the magnetization M_s within

*y-hibino@aist.go.jp

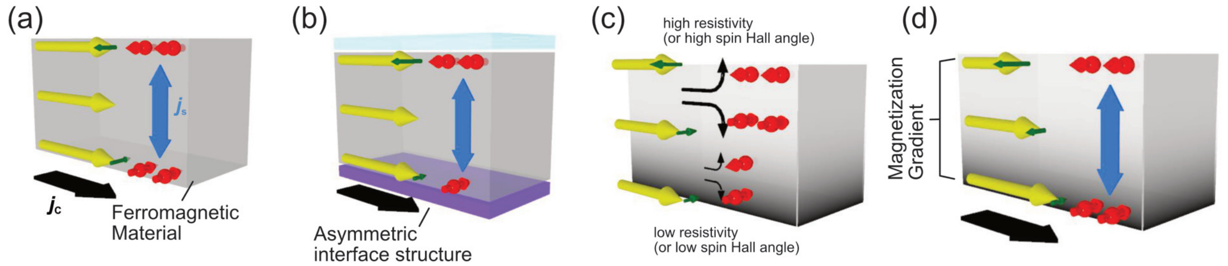

FIG. 1. Schematic of self-induced SOTs in ferromagnetic material (FM) with (a) inversion symmetry, (b) inversion asymmetry due to interface structure, (c) inversion asymmetry with gradient of spin Hall angle (or resistivity), and (d) inversion asymmetry with magnetization gradient. In-plane charge current j_c generates spin current j_s (blue or black arrows) along the out of plane direction resulting in accumulation of spin moment (red arrows). Spin transfer between local magnetic moment (yellow) and spin accumulation result in generation of self-induced SOTs (green arrows). Magnitude of local magnetic moment and self-induced SOTs are shown as varying lengths of arrows.

a FM. The SOT acting on the magnetic moment in a certain volume is inversely proportional to M_s. Therefore, when the inversion symmetry is broken by the gradient of M_s within the FM, the total self-induced SOTs remain finite in the FM [Fig. 1(d)]. To verify this idea, we quantitatively evaluated the SOT efficiency within the Ni-Fe alloy with a vertical gradient of M_s using spin-torque ferromagnetic resonance (STFMR). The gradient of M_s is introduced by forming a Ni composition gradient along the film deposition direction. Despite the use of heavy metal elements (e.g., Pt, Tb) within FMs [21–27,29,30], we show that not only the magnitude, but also the sign of the self-induced SOTs can be controlled by the direction of the gradient. We also propose a model to calculate self-induced SOTs under the vertical gradient of M_s, spin Hall angle, and resistivity, and we find that the spatial variation in M_s plays an important role in generating self-induced SOTs. Model calculations show that the self-induced SOTs of a FM with a M_s gradient can significantly enhance the SOT efficiency compared with those obtained from a uniform FM with interface asymmetry.

For this study, we deposited two magnetic stacks with two different types of vertical M_s gradient on a thermally oxidized Si substrate using an ultrahigh-vacuum magnetron sputtering system (Cannon-Anelva C-7100). Stacking structures were as follows [Fig. 2(a)]: Ta$-$B (t)/Ni $-$ Fe (5)/MgO/TaO_x (thickness in nanometers). The amorphous Ta-B ($Ta_{80}B_{20}$) layer acts as a buffer layer to improve the flatness of deposited films, and the thickness t was varied from 0 to 3 nm. The Ni-Fe layer consists of five layers with different Ni compositions which are Ni, $Ni_{87.5}Fe_{12.5}$, $Ni_{79.5}Fe_{20.5}$, $Ni_{70}Fe_{30}$, and $Ni_{48}Fe_{52}$. Note that the magnetic moment in Fe is larger than that of Ni, which results in a M_s gradient with Ni composition (see Supplemental Material [32]). In addition, we found that the resistivity ρ of the Ni-Fe alloy decreases with Ni composition [32]. We prepared two types of vertical gradient structure: One decreases the Ni composition from the substrate side (type A) and the other increases the Ni composition from the substrate side (type B). As for the reference structure, Ta-B $(t = 1, 2, 3)$/$Ni_{79.5}Fe_{20.5}$(5)/MgO/TaO_x, with a FM layer of uniform Ni composition, was also prepared. To verify the composition gradients of type A and B systems, we performed scanning electron microscopy (STEM) and energy-dispersive x-ray spectroscopy (EDXS) of type A and type B stacks with $t = 3$ nm which are shown in Figs. 2(b) and 2(c). The EDXS spectroscopy profiles along the vertical axis in both structures show an inhomogeneous distribution of Fe and Ni in the Ni-Fe layer. The EDXS intensity ratio of Fe to that of Ni (I_{Fe}/I_{Ni}) shows linear decrease (increase) in the type A (B) structure which is evidence of the presence of a vertical composition gradient in the Ni-Fe layer. The stacks were patterned as microstrip devices of 100 μm in length and 10 μm in width using conventional photolithography and Ar-ion milling. The electrical contacts were formed by depositing Cr (5 nm)/Au (160 nm) electrodes using the liftoff method.

To investigate the SOTs acting on the Ni-Fe layer, we conducted STFMR measurements [45–47]. A schematic of the measurement setup is shown in Fig. 3(a). We applied radio frequency (rf) current (I_{rf}) with GHz-order frequency to the microstrips and measured the rectified voltage V_{FMR} via the direct current (dc) port of bias T. The STFMR spectra were measured by sweeping a magnetic field H_{ext} under various in-plane angles φ. Figures 3(b) and 3(c) show the STFMR spectra of type A and B structures with $t = 3$ nm, respectively. In both structures, V_{FMR} was well fitted by the Lorentzian curve $V_{FMR} = V_S S(H_{ext}) + V_A A(H_{ext})$ which consists of a symmetric component $S(H_{ext})$ and an antisymmetric component $A(H_{ext})$. The Lorentzian fitting curves show that the sign of V_S and V_A is reversed by changing the gradient type. Note that the large difference in magnitude of V_A between the type A and B structures may originate from the offset of Oersted torque from the Ta-B buffer layer. The sign reversal of the V_S and V_A can be explained either by the sign reversal of R_{AMR} or of the SOTs acting on the Ni-Fe layer. We confirmed that $R_{AMR} > 0$ for both structures from the φ dependence of the device resistance as shown in the insets of Figs. 3(d) and 3(e). Therefore, the sign reversal and large modulation of the V_S and V_A between the two structures is attributable to the sign reversal of the SOTs. Furthermore, we performed an in-plane angular dependence study of the V_S and V_A in both systems, as shown in Figs. 3(d) and 3(e). The angular dependencies of $V_{S(A)}$ in both systems are well fitted by a $\cos^2\varphi \sin\varphi$ function, indicating that the SOTs acting on both systems have the same symmetry with the spin Hall effect [47]. Note that the spin Hall effect in the Ta-B buffer layer [48] does not result in sign reversal of the SOTs because the buffer layer is fixed to the bottom of the Ni-Fe layer in both structures. As a quantitative study, we estimated the efficiencies of the dampinglike component of the SOT

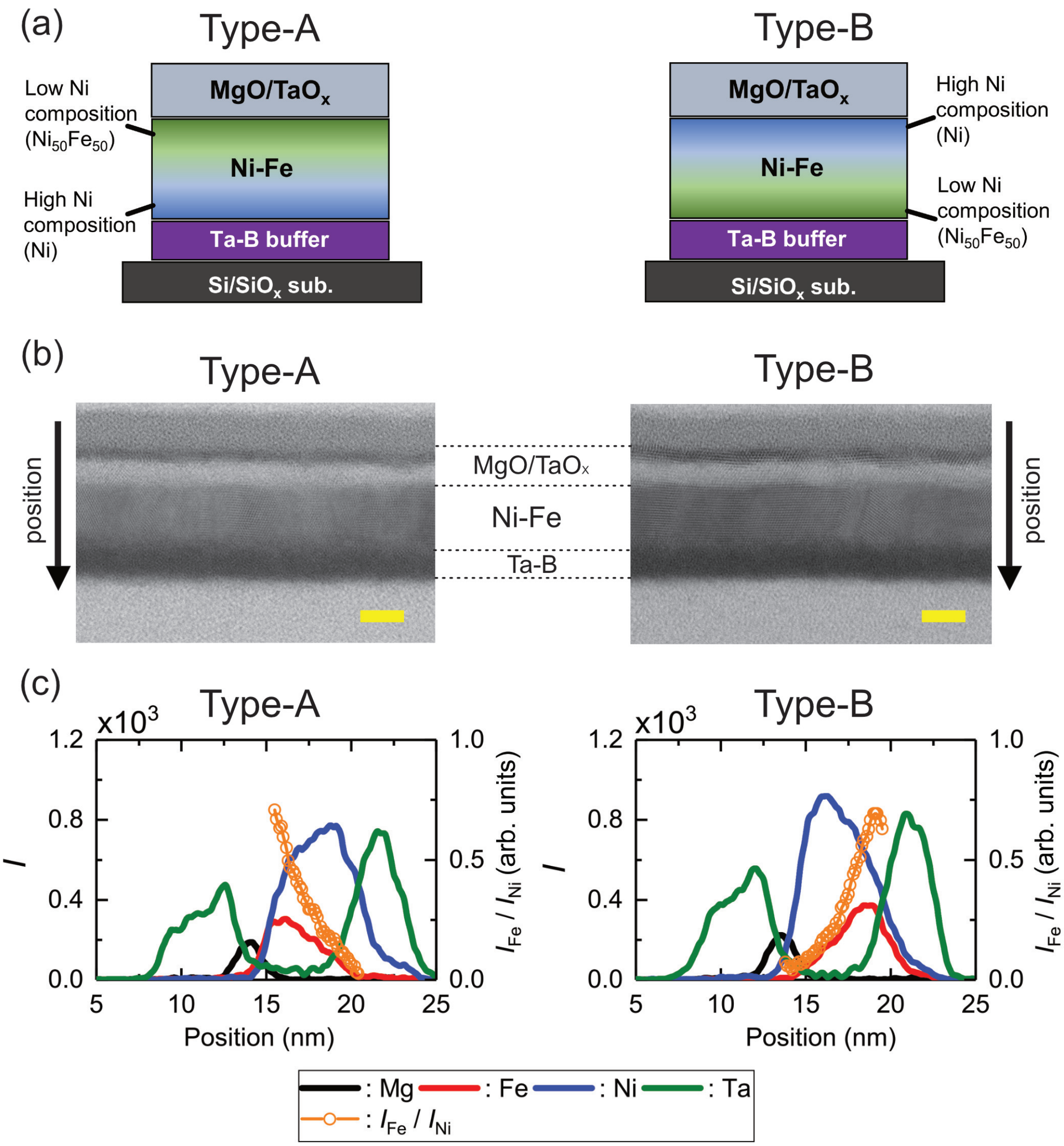

FIG. 2. (a) Schematic of magnetic stacks. Ni composition in Ni-Fe layer in type A(B) stack decrease (increase) composition gradient from the substrate side to the MgO interface. (b) STEM image of two samples. The yellow bar shows the scale bar of 2.5 nm. (c) EDXS vertical profile of Mg, Fe, Ni, and Ta in type A (left) and B (right) stack. Right axis represents the EDXS intensity ratio of Fe to that of Ni ($I_{\mathrm{Fe}}/I_{\mathrm{Ni}}$).

(sum of the fieldlike component of the SOT and the Oersted torque) per unit applied electric field ξ^E_{DL} ($\xi^E_{\mathrm{FL+Oe}}$) using the φ dependence of $V_{\mathrm{S}}(V_{\mathrm{A}})$ [46,47]. It should be noted that the Oersted torque contribution originates from two factors. One is from the Ta-B buffer layer, and the other is from an inhomogeneous current distribution within the Ni-Fe layer due to the resistivity gradient [32]. We estimated ξ^E_{DL} ($\xi^E_{\mathrm{FL+Oe}}$) in type A and B structures to be 32700 ± 600 (38600 ± 200) $\Omega^{-1}\,\mathrm{m}^{-1}$ and -46800 ± 700 (-3500 ± 400) $\Omega^{-1}\,\mathrm{m}^{-1}$, respectively. We note that the efficiencies of the dampinglike component of SOT per unit applied current density (ξ^j_{DL}) in type A (B) structures is estimated to be 2.2% (–2.5%) which is comparable to that of Co-Pt [22–24] and Co-Tb [31] with a composition gradient, although no heavy metal elements were used in this study. Moreover, ξ^j_{DL} is an order of magnitude larger than that of a uniform Ni-Fe single layer with asymmetric interfaces [21].

Let us now discuss the origins of self-induced SOTs in the present system. We consider four contributions. The first one arises from the interfacial asymmetry at the top (Ni-Fe/MgO) and bottom (Ta-B/Ni-Fe) surfaces. This contribution is similar to that discussed in Refs. [19,21]. The second and third possible origins can be attributed to the vertical gradients of spin Hall angle and resistivity due to the compositional gradient [27]. The last one is the vertical gradient of the magnetization, which is proposed in this work. For the first three origins, each component of spin accumulation $\boldsymbol{\mu}$ becomes asymmetric with respect to the FM center due to the different boundary condition or the spatial variations of the transport parameters (spin Hall angle or resistivity). SOTs originate from an exchange interaction between the spin accumulation and local magnetization [49]. Therefore, a local SOT, acting on the magnetic moments in a volume ΔV, is proportional to $\boldsymbol{\mu} \times \mathbf{m}/(M_s \Delta V)$, where $\mathbf{m}$ is the unit vector pointing in the direction of the local

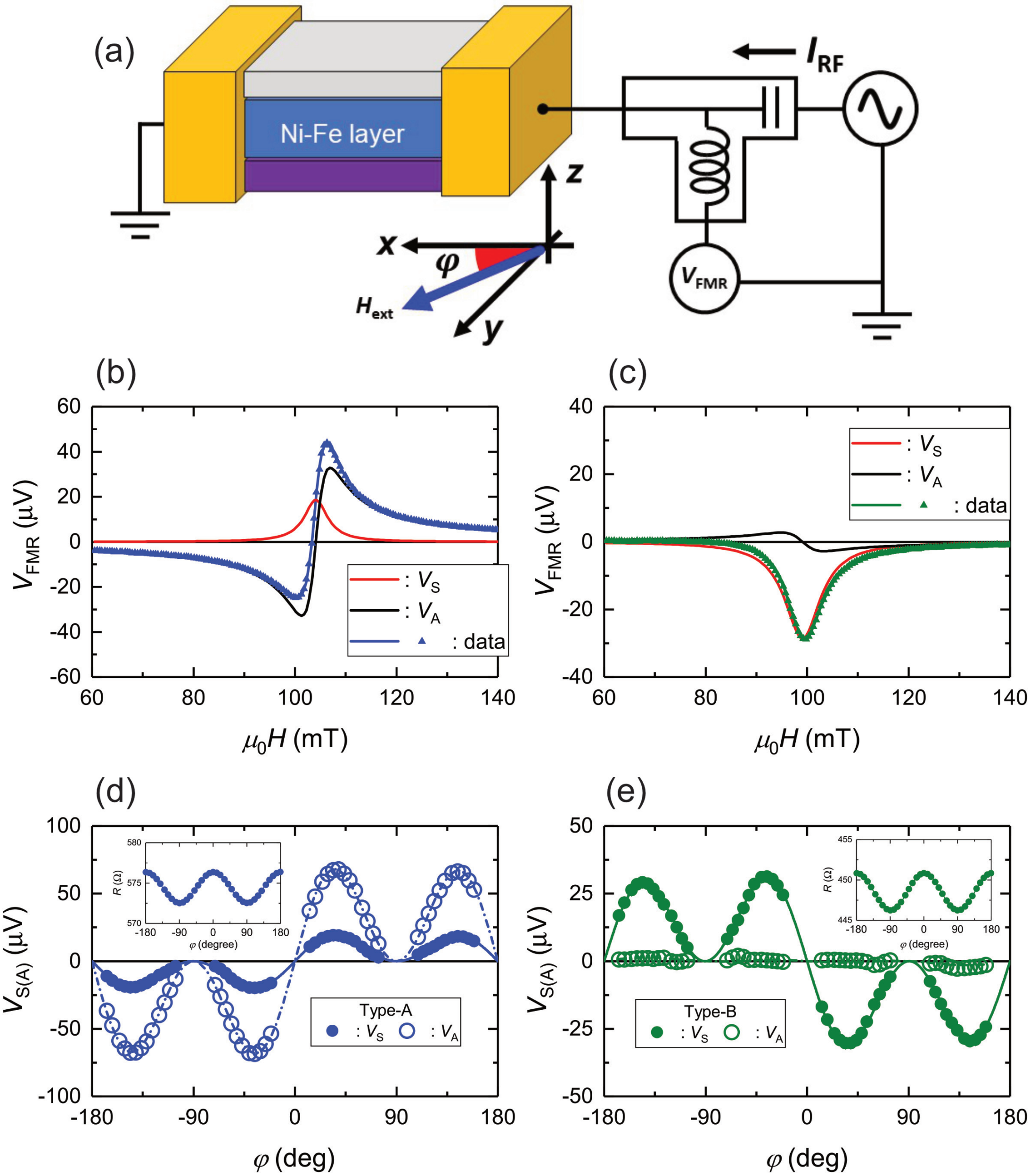

FIG. 3. (a) Schematic of measurement setup for STFMR. (b), (c) STFMR spectra for (b) type A and (c) type B stacks with $t = 3$ nm. In-plane angle (φ) and applied microwave frequency (f) are set to 45 ° and 10 GHz, respectively. Red and black solid curves show V_S and V_A components of Lorentzian fitting, respectively. (d), (e) φ dependence of V_s (solid symbol) and V_A (open symbol) for (d) type A and (e) type B sample with $t = 3$ nm. Solid and dotted curves denote fitting results. Inset of (d), (e) show the φ dependence of device resistance R for each structure.

magnetic moment. Because of the asymmetric distribution of the spin accumulation, the total SOT, which is an average of the local SOTs over the FM layer, remains finite. For the fourth origin, the magnitude of SOTs varies spatially due to the variation in M_s. This is because the magnitude of the SOT is determined by the transferred spin angular momentum per magnetic moment, which is mathematically represented by the factor $1/(M_s \Delta V)$. Therefore, self-induced SOTs via the M_s gradient can be generated even if the asymmetric profile of $\boldsymbol{\mu}$ is negligible.

To compare these origins, we quantified the self-induced SOTs from drift-diffusion spin transport theory [49] with additional terms originating from the compositional gradient. The calculation details are summarized in the Supplemental Material [32]. The basic structure consists of a nonmagnetic spin-sink layer, the FM layer, and an oxide layer, as schematically shown in Fig. 4(a). To evaluate the contributions of the four origins mentioned above to the self-induced SOTs, we set the values of the parameters in this structure comprehensively, as summarized in Table I. In case I, the magnetization M_s, spin Hall angle θ_{SHE}, and resistivity ρ are spatially uniform in FMs. In the other cases, we introduce the spatial gradient of M_s (case II), θ_{SHE} (case III), and ρ (case IV) in FMs. For each case, we consider two directions of the gradient,

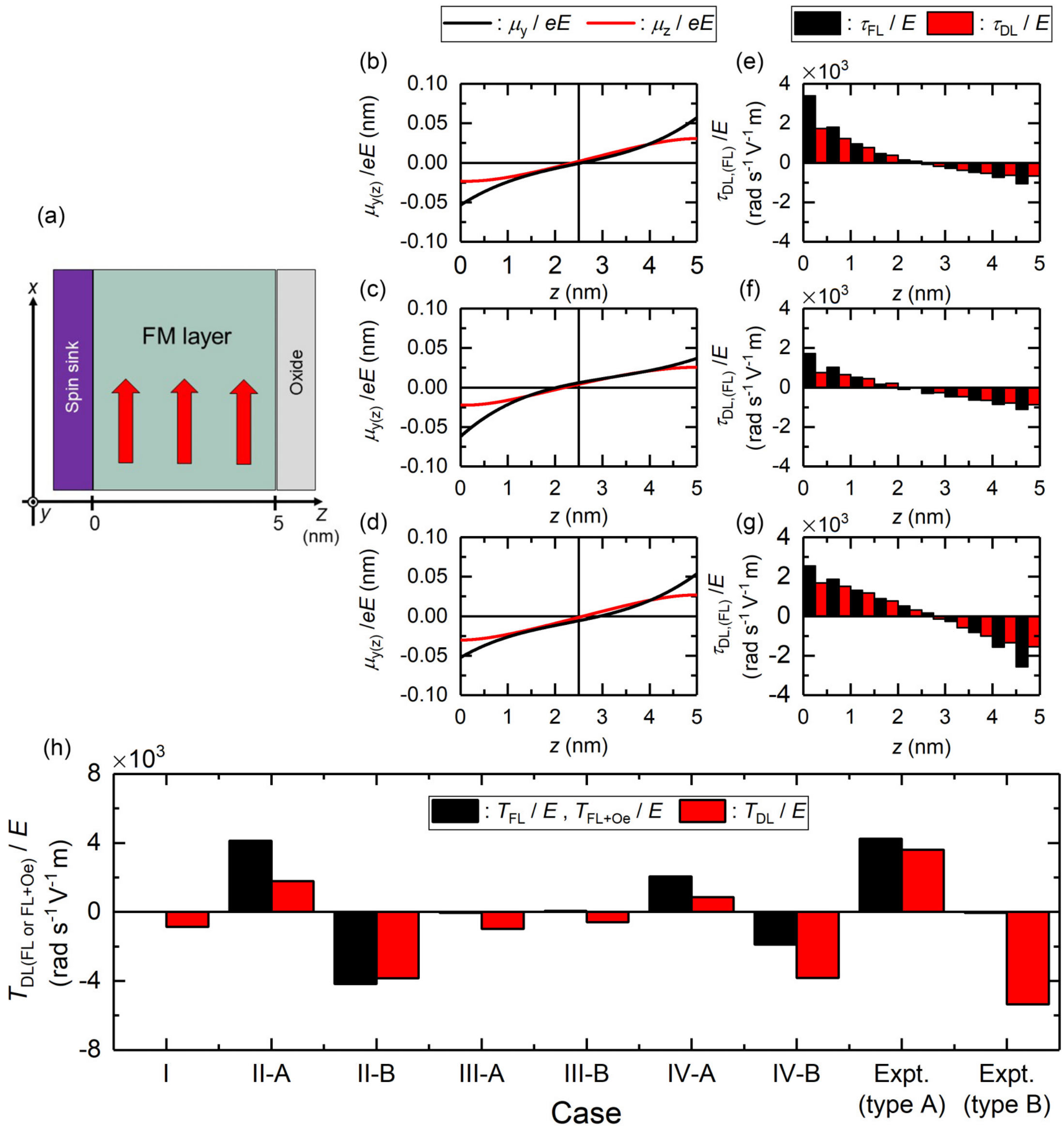

FIG. 4. (a) Schematic of proposed model system consisting of nonmagnetic spin-sink layer/FM/oxide layer. Red arrow shows the magnetization pointing along the $+x$ direction in the calculation. Charge current flow direction is set to the $+x$ direction. (b–d) Spin accumulation ($\mu_{y(z)}/eE$) profile in FM layer for (b) case II-A, (c) case III-A, and (d) case IV-A. (e–g) Calculated t_{DL}/E and t_{FL}/E profile in FM layer for (e) case II-A, (f) case III-A, and (g) case IV-A. (h) Torque efficiency of self-induced SOTs (T_{DL}/E and $T_{FL(FL+Oe)}/E$) for each calculation case and experimental results in type-A and type-B structure for $t = 3$ nm devices shown in Fig. 3. Black and red represent the fieldlike and dampinglike components of self-induced SOTs ($T_{FL(FL+Oe)}/E$ and T_{DL}/E, respectively).

TABLE I. A summary of M_s, θ_{SHE}, and ρ of the various cases used in model calculation. Cases I–IV correspond to the FM layer with uniform parameter, the FM layer introducing the spatial gradient of M_s, the FM layer introducing he spatial gradient of θ_{SHE}, and the FM layer introducing the spatial gradient of ρ, respectively. "-A" and "-B" correspond to the gradient direction that matches the type A and type B structures used in STFMR measurements.

Case	M_s (emu/cm^3)	θ_{SHE} (arb. units)	ρ(μΩ cm)
I	750	0.022	50
II-A	300 ($z = 0$ nm), 1200 ($z = 5$ nm)	0.022	50
II-B	1200 ($z = 0$ nm), 300 ($z = 5$ nm)	0.022	50
III-A	750	0.03 ($z = 0$ nm), 0.01 ($z = 5$ nm)	50
III-B	750	0.01 ($z = 0$ nm), 0.03 ($z = 5$ nm)	50
IV-A	750	0.022	30 ($z = 0$ nm), 70 ($z = 5$ nm)
IV-B	750	0.022	70 ($z = 0$ nm), 30 ($z = 5$ nm)

distinguished by the labels "A" and "B." The values of M_s and ρ are estimated from the present experiment [32]. The value of θ_{SHE} is derived from the previous reports for Ni ($\theta_{SHE} = 0.03$) and Fe ($\theta_{SHE} = -0.01$) [11]. Figures 4(b)–4(d) show the spatial profile of the spin accumulation in case II-A, III-A, and IV-A. Note that the spin accumulation for cases I and II-B is same as that of case II-A. Here $\mu_{y(z)}$ is the spin accumulation in the $y(z)$-axis direction for which the coordination is shown in Fig. 4(a). In case II-A, the profiles of the spin accumulations are approximately symmetric with respect to the center of the FM, even though the interfaces are asymmetric. This result suggests that the contribution of the interfacial asymmetry to the self-induced SOT is small. On the other hand, in cases III-A and IV-A, the profiles of the spin accumulations are asymmetric with respect to the FM center. This is because the spatial variations of the spin Hall angle and the resistivity result in spatially asymmetric generation of spin accumulations.

Next we evaluated the local SOTs, $\boldsymbol{\mu} \times \mathbf{m}/(M_s \Delta V)$, in units of angular frequency and per electric field E with a 0.5 nm step. The results are shown in Figs. 4(e)–4(g) for cases II-A, III-A, and IV-A. The dampinglike and fieldlike components of the local SOTs correspond to τ_{DL}/E and τ_{FL}/E, respectively. We note that the profile of the local SOT for case II-A is significantly asymmetric, even though the spatial profile of the spin accumulations is approximately symmetric. This asymmetric SOT originates from the spatial variation of M_s. The asymmetric profiles of the local SOTs for cases III-A and IV-A arise from the spatial variation of the spin accumulations. The sums of these local SOTs, $T_{DL(FL)}/E = \sum \tau_{DL(FL)}/E$, are summarized in Fig. 4(h), which correspond to the SOT efficiencies measured by the experiments. Comparing these values with the experimental results, we first notice that the interfacial asymmetry in case I is negligible. On the other hand, large $T_{DL(FL)}/E$ and its sign reversal with the gradient direction are observed in case II (M_s gradient) and case IV (ρ gradient). Note also that the torque efficiencies in these cases agree with the experimental results. The torque efficiencies for cases III-A and III-B show no sign reversal of T_{DL}/E which indicate that the SOT induced by the θ_{SHE} gradient is negligibly small compared with the SOT induced by the interfacial asymmetry. The magnitude of the SOT efficiency induced by the θ_{SHE} gradient, which corresponds to the difference of $T_{DL(FL+Oe)}/E$ between cases III-A and III-B, is approximately one order of magnitude smaller than that of cases II and IV, as well as the experimental results. Furthermore, comparing cases II and IV, the torque efficiency in case II is larger than that in case IV. We also calculated $T_{DL(FL+Oe)}/E$ considering both the M_s and θ_{SHE} gradients. However, the calculated results did not change much compared to case II. Summarizing these results, we conclude that the spatial gradient of M_s is the dominant contribution to the self-induced SOT in the present system. We notice that the self-induced SOT due to the gradient of M_s provides an appropriate sign even when the model is applied to Co-Pt and Fe-Pt systems [23,27] where M_s decreases with increasing Pt composition. In the case of ferrimagnets, such as Co-Tb and Gd-Fe-Co, SOT rapidly increases in the vicinity of the compensation point where M_s approaches ~ 0. Therefore, self-induced SOT in ferrimagnets is governed by the local SOT acting on the region in the vicinity of the compensation point [50,51] which can also qualitatively explain the sign reversal of self-induced SOT with the gradient direction [31]. Lastly, we note that other parameters, such as the spin diffusion length, may also vary spatially and lead to a self-induced SOT. An investigation of such possibilities will form part of our future work.

We now discuss the other possible effects which may explain the sign reversal of SOTs observed in our experimental results besides that of self-induced SOTs. One is the Rashba-Edelstein effect induced SOTs from the top and bottom interfaces [52,53]. The second is the current-induced torque originating from the orbit Hall effect from the Ta-B buffer layer, namely, orbital torques (OTs) [54–57]. To examine these effects, we investigated the Ta-B thickness t in type A and B structures. Especially in the case of $t = 0$ nm, the top and bottom interface structures were more symmetrical than when $t \neq 0$. The contribution of OT can also be eliminated in the $t = 0$ structure because there would be no orbital Hall effect from the Ta-B layer. Figures 5(a) and 5(b) show the STFMR spectra of type A and B structures with $t = 0$, respectively. A sizable V_s was observed in both structures indicating the existence of a sizable dampinglike component of SOT efficiency despite the absence of a nonmagnetic buffer layer. Moreover, the sign of V_S is reversed upon the gradient direction which indicates that the sign reversal of SOTs acting on the Ni-Fe layer does not contribute to either SOTs induced by the Rashba-Edelstein effect or OTs, but rather to the self-induced SOT acting within the Ni-Fe layer. Figures 5(c) and 5(d) show the Ta-B thickness (t) dependence of ξ_{DL}^E and ξ_{FL+Oe}^E in type A, type B, and the reference structures, respectively. The STFMR spectra and φ dependence of V_S and V_A for each t and structures are summarized in the Supplemental Material [32]. The estimated $|\xi_{DL}^E|$ and $|\xi_{FL+Oe}^E|$ in the reference structure show lower values compared to the type A and type B structures, which is also consistent with the calculation result of case I shown in Fig. 4(h). We note that a slight sign reversal of ξ_{DL}^E in the reference structure with $t = 1$ nm was observed which we speculate is due to an interfacial contribution [52,53]. To extract the contribution of spin Hall effect induced SOTs from the Ta-B layer, we plotted the differential of ξ_{DL}^E between type A and type B structure, shown in red plot. The differential data of ξ_{DL}^E increased rapidly with t and saturated at ~ 2 nm. The differential data of ξ_{FL+Oe}^E show almost constant in $t \neq 0$ nm. The rapid enhancement of differential ξ_{DL}^E with t can be explained by the asymmetric spin accumulation profile within the Ni-Fe layer via insertion of Ta-B buffer layer. Previous studies have reported that torque efficiency of OTs does not saturate in such a short thickness region [56–58]. This is because the diffusion length of the orbital angular momentum is much longer than that of the spin angular momentum. Therefore, our results, which show rapid saturation of ξ_{DL}^E, further support that the observed SOTs are not attributed to OTs but to self-induced SOTs.

In conclusion, we have experimentally demonstrated that the composition gradient in Ni-Fe alloy significantly modulates the magnitude and sign of the self-induced SOTs. The torque efficiency of the dampinglike torque in two different gradient structures measured by the STFMR experiments were estimated to be $32\,700 \pm 600$ and $-46\,800 \pm 700\ \Omega^{-1}\ \mathrm{m}^{-1}$, depending on the direction of the composition gradient. These values are comparable to previous results

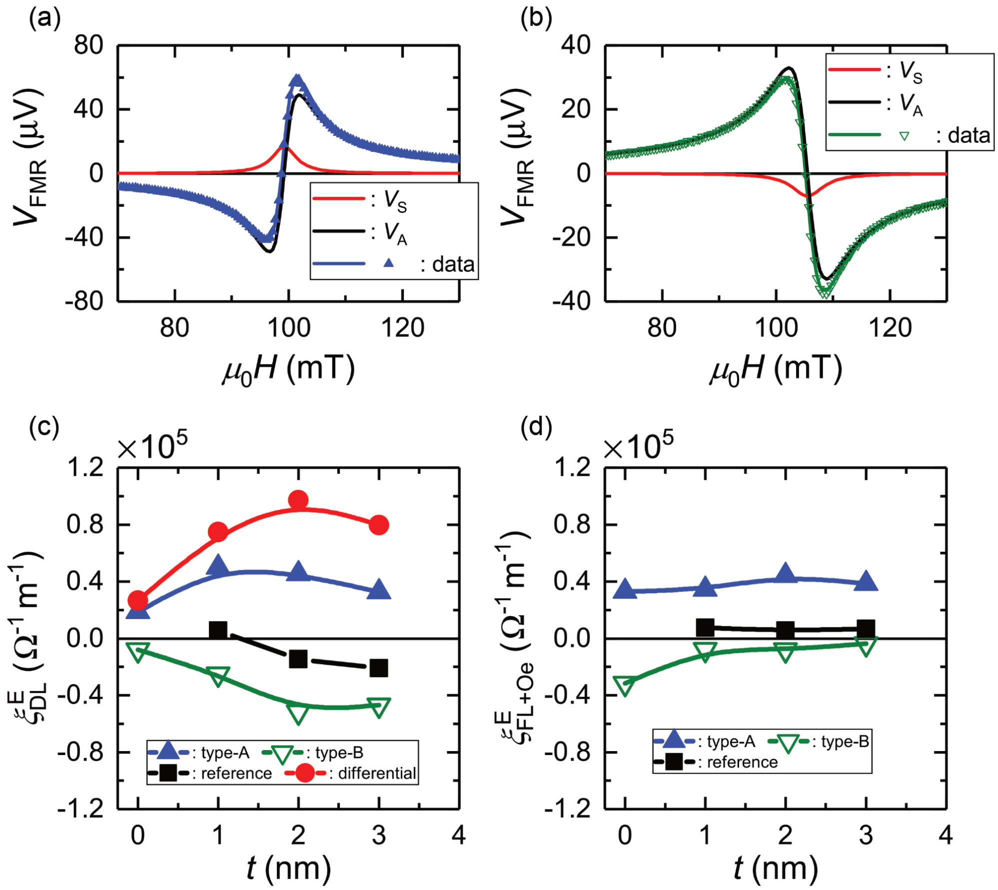

FIG. 5. STFMR spectra for (a) type A and (b) type B sample with no Ta-B buffer layer. Measurement parameters are the same as in Figs. 2(b) and 2(c). (c), (d) Ta-B buffer layer thickness dependence of (c) $\xi^E_{\rm DL}$ and (d) $\xi^E_{\rm FL+Oe}$ for type A (blue solid symbol), type B (green open symbol), and differential $\xi^E_{\rm DL}$ between types A and B (red circle symbol). The solid curves are guides for the eye. Black square symbols show $\xi^E_{\rm DL}$ and $\xi^E_{\rm FL+Oe}$ for reference structure with uniform Ni composition.

from composition gradients using heavy metal elements, even though no heavy metal elements were used. We have also proposed an alternative origin of these torques, namely, the gradient of the magnetization. Since the SOT strength is the spin angular momentum per magnetic moment and is transferred from the spin accumulation, the spatial variation of the magnetization results in that of the local SOT and, thus, the total SOT remains finite. We have examined the contribution of the spatial variation of the magnetization to the self-induced SOTs by developing a spin transport theory and compared it to other contributions, such as the interfacial asymmetry and spatial gradient of spin Hall angle and resistivity. Using the experimental values, we have calculated the SOTs for various cases and found that the spatial variation of the magnetization provides the dominant contribution to the SOTs. These findings show quantitative agreement with the experiments and qualitatively explain previous reports. These results show that the magnetization gradient can be an alternative origin to generate a finite self-induced SOT which could be useful for realizing energy-efficient SOT-based devices.

The authors thank S. Tamaru, T. Yamamoto, and A. Spiesser for technical support and valuable discussions. This work is supported by JSPS KAKENHI (Grant No. 23H01477) and partially supported by the JST-Mirai Program (Grant No. JPMJMI20A1), and the JST-CREST Program (Grant No. JPMJCR18T3). A part of this work was conducted at the AIST Nano-Processing Facility supported by the "Nanotechnology Platform Program" of the Ministry of Education, Culture, Sports, Science and Technology (MEXT), Japan.

[1] R. Ramaswamy, J. M. Lee, K. Cai, and H. Yang, Recent advances in spin-orbit torques: Moving towards device applications, Appl. Phys. Rev. **5**, 031107 (2018).

[2] X. Qiu, Z. Shi, W. Fan, S. Zhou, and H. Yang, Characterization and manipulation of spin orbit torque in magnetic heterostructures, Adv. Mater. **30**, 1705699 (2018).

[3] A. Manchon, J. Železný, I. M. Miron, T. Jungwirth, J. Sinova, A. Thiaville, K. Garello, and P. Gambardella, Current-induced spin-orbit torques in ferromagnetic and antiferromagnetic systems, Rev. Mod. Phys. **91**, 035004 (2019).

[4] J. Ryu, S. Lee, K.-J. Lee, and B.-G. Park, Current-induced spin-orbit torques for spintronic applications, Adv. Mater. **32**, 1907148 (2020).

[5] I. M. Miron, K. Garello, G. Gaudin, P. J. Zermaten, M. V. Costache, S. Auffret, S. Bandiera, B. Rodmacq, A. Schuhl, and P. Gambardella, Perpendicular switching of a single ferromagnetic layer induced by in-plane current injection, Nature (London) **476**, 189 (2011).

[6] L. Liu, C.-F. Pai, Y. Li, H. W. Tseng, D. C. Ralph, and R. A. Buhrman, Spin-torque switching with the giant spin Hall effect of Tantalum, Science **336**, 555 (2012).

[7] B. F. Miao, S. Y. Huang, D. Qu, and C. L. Chien, Inverse spin Hall effect in a ferromagnetic metal, Phys. Rev. Lett. **111**, 066602 (2013).

[8] A. Tsukahara, Y. Ando, Y. Kitamura, H. Emoto, E. Shikoh, M. P. Delmo, T. Shinjo, and M. Shiraishi, Self-induced inverse spin Hall effect in permalloy at room temperature, Phys. Rev. B **89**, 235317 (2014).

[9] C. Du, H. Wang, F. Yang, and P. C. Hammel, Systematic variation of spin-orbit coupling with d-orbital filling: Large inverse spin Hall effect in 3d transition metals, Phys. Rev. B **90**, 140407(R) (2014).

[10] H. Wang, C. Du, P. C. Hammel, and F. Yang, Spin current and inverse spin Hall effect in ferromagnetic metals probed by $Y_3Fe_5O_{12}$−based spin pumping, Appl. Phys. Lett. **104**, 202405 (2014).

[11] Y. Omori, E. Sagasta, Y. Niimi, M. Gradhand, L. E. Hueso, F. Casanova, and Y.-C. Otani, Relation between spin Hall effect and anomalous Hall effect in 3d ferromagnetic metals, Phys. Rev. B **99**, 014403 (2019).

[12] Y. Hibino, K. Yakushiji, A. Fukushima, H. Kubota, and S. Yuasa, Spin-orbit torque generated from perpendicularly magnetized Co/Ni multilayers, Phys. Rev. B **101**, 174441 (2020).

[13] Y. Hibino, T. Taniguchi, K. Yakushiji, A. Fukushima, H. Kubota, and S. Yuasa, Giant charge-to-spin conversion in ferromagnet via spin-orbit coupling, Nat. Commun. **12**, 6254 (2021).

[14] A. M. Humphries, T. Wang, E. R. Edwards, S. R. Allen, J. M. Shaw, H. T. Nembach, J. Q. Xiao, T. J. Silva, and X. Fan, Observation of spin-orbit effects with spin rotation symmetry, Nat. Commun. **8**, 911 (2017).

[15] S.-H. C. Baek, V. P. Amin, Y.-W. Oh, G. Go, S.-J. Lee, G.-H. Lee, K.-J. Kim, M. D. Stiles, B.-G. Park, and K.-J. Lee, Spin currents and spin-orbit torques in ferromagnetic trilayers, Nat. Mater. **17**, 509 (2018).

[16] S. Iihama, T. Taniguchi, K. Yakushiji, A. Fukushima, Y. Shiota, S. Tsunegi, R. Hiramatsu, S. Yuasa, Y. Suzuki, and H. Kubota, Spin-transfer torque induced by the spin anomalous Hall effect, Nat. Electron. **1**, 120 (2018).

[17] C. Safranski, E. A. Montoya, and I. N. Krivorotov, Spin-orbit torque driven by a planar Hall current, Nat. Nanotechnol. **14**, 27 (2019).

[18] A. Chernyshov, M. Overby, X. Liu, J. K. Furdyna, Y. Lyanda-Geller, and L. P. Rokhinson, Evidence for reversible control of magnetization in a ferromagnetic material by means of spin-orbit magnetic field, Nat. Phys. **5**, 656 (2009).

[19] W. Wang, T. Wang, V. P. Amin, Y. Wang, A. Radhakrishnan, A. Davidson, S. R. Allen, T. J. Silva, H. Ohldag, D. Balzar, B. L. Zink, P. M. Haney, J. Q. Xiao, D. G. Cahill, V. O. Lorenz, and X. Fan, Anomalous spin-orbit torques in magnetic single-layer films, Nat. Nanotechnol. **14**, 819 (2019).

[20] M. Haider, A. A. Awad, M. Dvornik, R. Khymyn, A. Houshang, and J. Åkerman, A single layer spin-orbit torque nano-oscillator, Nat. Commun. **10**, 2362 (2019).

[21] T. Seki, Y.-C. Lau, S. Iihama, and K. Takanashi, Spin-orbit torque in a Ni-Fe single layer, Phys. Rev. B **104**, 094430 (2021).

[22] L. Zhu, X. S. Zhang, D. A. Muller, D. C. Ralph, and R. A. Buhrman, Observation of strong bulk damping-like spin-orbit torque in chemically disordered ferromagnetic single layers, Adv. Funct. Mater. **30**, 2005201 (2020).

[23] X. Xie, X. Zhao, Y. Dong, X. Qu, K. Aheng, X. Han, X. Han, Y. Fan, L. Bai, Y. Chen, Y. Dai, Y. Tian, and S. Yan, Controllable field-free switching of perpendicular magnetization through bulk spin-orbit torque in symmetry-broken ferromagnetic films, Nat. Commun. **12**, 2473 (2021).

[24] Z. Chen, L. Liu, Z. Ye, Z. Chen, H. Zheng, W. Jia, Q. Zeng, N. Wang, B. Xiang, T. Lin, J. Liu, M. Qiu, S. Li, J. Shi, P. Han, and H. An, Current-induced magnetization switching in a chemically disordered A1 CoPt single layer, Appl. Phys. Express **14**, 033002 (2021).

[25] S. Q. Zheng, K. K. Meng, Q. B. Liu, J. K. Chen, J. Miao, X. G. Xu, and Y. Jiang, Disorder dependent spin-orbit torques in $L1$ FePt single layer, Appl. Phys. Lett. **117**, 242403 (2020).

[26] L. Liu, J. Yu, R. González-Hernández, C. Li, J. Deng, W. Lin, C. Zhou, T. Zhou, J. Zhou, H. Wang, R. Guo, H. Y. Yoong, G. M. Chow, X. Han, B. Dupé, J. Železný, J. Sinova, and J. Chen, Electrical switching of perpendicular magnetization in a single ferromagnetic layer, Phys. Rev. B. **101**, 200402(R) (2020).

[27] M. Tang, K. Shen, S. Zu, H. Yang, S. Hu, W. Lu, C. Li, M. Li, Z. Yuan, S. J. Pennycook, K. Xia, A. Manchon, S. Zhou, and X. Qiu, Bulk spin torque-driven perpendicular magnetization switching in $L10$ FePt single layer, Adv. Mater. **32**, 2002607 (2020).

[28] L. Zhu, D. C. Ralph, and R. A. Buhrman, Unveiling the mechanism of bulk spin-orbit torques within chemically disordered Fe_xPt_{1-x} single layers, Adv. Funct. Mater. **31**, 2103898 (2021).

[29] Z. Luo, Q. Zhang, Y. Zu, Y. Yang, X. Zhang, and Y. Wu, Spin-orbit torque in a single ferromagnetic layer induced by surface spin rotation, Phys. Rev. Appl. **11**, 064021 (2019).

[30] J. W. Lee, J. Y. Park, J. M. Yuk, and B. G. Park, Spin-orbit torque in a perpendicularly magnetized ferrimagnetic Tb-Co single layer, Phys. Rev. Appl. **13**, 044030 (2020).

[31] Z. Zhang, Y. Zhang, V. Lopez-Dominguez, L. Sanchez-Tejerina, J. Shi, X. Feng, L. Chen, Z. Wang, Z. Zhang, K. Zhang, B. Hong, Y. Xu, Y. Zhang, M. Carpentieri, A. Fert, G. Finocchio, W. Zhao, and P. K. Amiri, Field-free spin-orbit torque-induced switching of perpendicular magnetization in a ferrimagnetic layer with a vertical composition gradient, Nat. Commun. **12**, 4555 (2021).

[32] See Supplemental Material at http://link.aps.org/supplemental/10.1103/PhysRevB.109.L180409 for more details on Ni composition dependence of M_s and ρ, estimation of $\xi^E_{DL(FL+Oe)}$ and $T_{DL(FL)}/E$ from STFMR measurement, ferromagnetic resonance properties, estimation of rf current, model calculation of self-induced SOT, and angular dependence of V_S and V_A in various buffer layer thickness and structure type, which also includes Refs. [33–44].

[33] T. Gao, A. Qaiumzadeh, H. An, A. Musha, Y. Kageyama, J. Shi, and K. Ando, Intrinsic spin-orbit torque arising from the Berry curvature in a metallic-magnet/Cu-oxide interface, Phys. Rev. Lett. **121**, 017202 (2018).

[34] T. Taniguchi, J. Grollier, and M. D. Stiles, Spin-transfer torques generated by the anomalous Hall effect and anisotropic magnetoresistance, Phys. Rev. Appl. **3**, 044001 (2015).

[35] V. P. Amin and M. D. Stiles, Spin transport at interfaces with spin-orbit coupling: Formalism, Phys. Rev. B **94**, 104419 (2016).
[36] V. P. Amin and M. D. Stiles, Spin transport at interfaces with spin-orbit coupling: Phenomenology, Phys. Rev. B **94**, 104420 (2016).
[37] V. P. Amin, J. Zeeman, and M. D. Stiles, Interface-generated spin currents, Phys. Rev. Lett. **121**, 136805 (2018).
[38] V. P. Amin, J. Li, M. D. Stiles, and P. M. Haney, Intrinsic spin currents in ferromagnets, Phys. Rev. B **99**, 220405 (2019).
[39] K.-W. Kim and K.-J. Lee, Generalized spin drift-diffusion formalism in the presence of spin-orbit interaction of ferromagnets, Phys. Rev. Lett. **125**, 207205 (2020).
[40] T. Taniguchi and H. Imamura, Spin pumping in ferromagnetic multilayers, Mod. Phys. Lett. B **22**, 2909 (2008).
[41] L. Liu, O. J. Lee, T. J. Gudmundsen, D. C. Ralph, and R. A. Buhrman, Current-induced switching of perpendicularly magnetized magnetic layers using spin torque from the spin Hall effect, Phys. Rev. Lett. **109**, 096602 (2012).
[42] S. Maekawa, S. O. Valenzuela, E. Saitoh, and T. Kimura, *Spin Current* (Oxford University Press, Oxford, 2012).
[43] A. Brataas, Y. V. Nazarov, and G. E. W. Bauer, Spin-transport in multi-terminal normal metal-ferromagnet systems with non-collinear magnetizations, Eur. Phys. J. B **22**, 99 (2001).
[44] T. Taniguchi, S. Yakata, H. Imamura, and Y. Ando, Determination of penetration depth of transverse spin current in ferromagnetic metals by spin pumping, Appl. Phys. Express **1**, 031302 (2008).
[45] L. Liu, T. Moriyama, D. C. Ralph, and R. A. Buhrman, Spin-torque ferromagnetic resonance induced by the spin Hall effect, Phys. Rev. Lett. **106**, 036601 (2011).
[46] D. Fang, H. Kurebayashi, J. Wunderlich, K. Vyborny, L. Zarbo, R. P. Campion, A. Casiraghi, B. L. Gallagher, T. Jungwirth, and A. J. Ferguson, Spin-orbit-driven ferromagnetic resonance, Nat. Nanotechnol. **6**, 413 (2011).
[47] D. MacNeill, G. M. Stiehl, M. H. D. Guimaraes, R. A. Buhrman, J. Park, and D. C. Ralph, Control of spin-orbit torques through crystal symmetry in WTe_2/ferromagnet bilayers, Nat. Phys. **13**, 300 (2017).
[48] Y. Kato, Y. Saito, H. Yoda, T. Onokuchi, S. Shirotori, N. Shimomura, S. Oikawa, A. Tiwari, M. Ishikawa, M. Shimizu, B. Altansargai, H. Sugiyama, K. Koi, Y. Ohsawa, and A. Kurobe, Improvement of write efficiency in voltage-controlled spintronic memory by development of a Ta-B spin Hall electrode, Phys. Rev. Appl. **10**, 044011 (2018).
[49] S. Zhang, P. M. Levy, and A. Fert, Mechanisms of spin-polarized current-driven magnetization switching, Phys. Rev. Lett. **88**, 236601 (2002).
[50] J. Finley and L. Q. Liu, Spin-orbit-torque efficiency in compensated ferrimagnetic cobalt-terbium alloys, Phys. Rev. Appl. **6**, 054001 (2016).
[51] W. S. Ham, S. Kim, D. H. Kim, K. J. Kim, T. Okuno, H. Yoshikawa, A. Tsukamoto, T. Moriyama, and T. Ono, Temperature dependence of spin-orbit effective fields in Pt/GdFeCo bilayers, Appl. Phys. Lett. **110**, 242405 (2017).
[52] G. Allen, S. Manipatruni, D. E. Nikonov, M. Doczy, and I. A. Young, Experimental demonstration of the coexistence of spin Hall and Rashba effects in β-tantalum/ferromagnet bilayers, Phys. Rev. B **91**, 144412 (2015).
[53] S. Emori, T. Nan, A. M. Belkessam, X. Wang, A. D. Matyushov, C. J. Babroski, Y. Gao, H. Lin, and N. X. Sun, Interfacial spin-orbit torque without spin-orbit coupling, Phys. Rev. B **93**, 180402(R) (2016).
[54] D. Lee, D. Go, H.-J. Park, W. Jeong, W.-W. Ko, D. Yun, D. Jo, G. Go, J. H. Oh, K.-J. Kim, B.-G. Park, B.-C. Min, H. C. Koo, H.-W. Lee, O. Lee, and K.-J. Lee, Orbital torque in magnetic bilayers, Nat. Commun. **12**, 6710 (2021).
[55] G. Sala and P. Gambardella, Giant orbital Hall effect and orbital-to-spin conversion in $3d$, $5d$, and $4f$ metallic heterostructures, Phys. Rev. Res. **4**, 033037 (2022).
[56] H. Hayashi, D. Jo, D. Go, T. Gao, S. Haku, Y. Mokrousov, H. W. Lee, and K. Ando, Observation of long-range orbital transport and giant orbital torque, Commun. Phys. **6**, 32 (2023).
[57] R. Fukunaga, S. Haku, H. Hayashi, and K. Ando, Orbital torque originating from orbital Hall effect in Zr, Phys. Rev. Res. **5**, 023054 (2023).
[58] Y.-G. Choi, D. Jo, K.-H. Ko, D. Go, K.-H. Kim, H. G. Park, C. Kim, B.-C. Min, G.-M. Choi, and H.-W. Lee, Observation of the orbital Hall effect in a light metal Ti, Nature (London) **619**, 52 (2023).